

Cite this: *Phys. Chem. Chem. Phys.*, 2011, **13**, 19553–19560

www.rsc.org/pccp

PAPER

A novel tungsten trioxide (WO₃)/ITO porous nanocomposite for enhanced photo-catalytic water splitting

Hidetaka Ishihara,^a Ganesh K. Kannarpady,^{*a} Khedir R. Khedir,^a Justin Woo,^a Steve Trigwell^b and Alexandru S. Biris^{*a}

Received 4th August 2011, Accepted 9th September 2011

DOI: 10.1039/c1cp22856k

Hybrid nanocomposite films of ITO-coated, self-assembled porous nanostructures of tungsten trioxide (WO₃) were fabricated using electrochemical anodization and sputtering. The morphology and chemical nature of the porous nanostructures were studied by Scanning Electron Microscopy (SEM) and X-ray Photoelectron Spectroscopy (XPS), respectively. The photoelectrochemical (PEC) properties of WO₃ porous nanostructures were studied in various alkaline electrolytes and compared with those of titania nanotubes. A new type of alkaline electrolyte containing a mixture of NaOH and KOH was proposed for the first time to the best of our knowledge and shown to improve the photocurrent response of the photoanodes. Here, we show that both the WO₃ nanostructures and titania nanotubes (used for comparison) exhibit superior photocurrent response in the mixture of NaOH and KOH than in other alkaline electrolytes. The WO₃ porous nanostructures suffered from surface corrosion resulting in a huge reduction in the photocurrent density as a function of time in the alkaline electrolytes. However, with a protective coating of ITO (100 nm), the surface corrosion of WO₃ porous nanostructures reduced drastically. A tremendous increase in the photocurrent density of as much as 340% was observed after the ITO was applied to the WO₃ porous nanostructures. The results suggest that the hybrid ITO/WO₃ nanocomposites could be potentially coupled with titania nanotubes in a multi-junction PEC cell to expand the light absorption capability in the solar spectrum for water splitting to generate hydrogen.

Introduction

A photoelectrochemical (PEC) solar cell is a device that absorbs solar radiation and splits water into hydrogen and oxygen electrochemically.¹ For the effective implementation of this technique, the photoelectrodes that absorb the solar radiation must satisfy several important conditions, such as photocorrosion stability, wavelength response in the solar spectrum, and cost effectiveness.^{2,3} The photoelectrodes with a wide band gap show higher photo-corrosion stability but suffer from a low light absorption in the solar spectrum. On the other hand, the photoelectrodes with a narrow band gap absorb a much wider spectrum of sunlight but suffer from poor corrosion stability.^{3,4} Hence, for the last few decades, the identification and selection of a photo-electrode material that could meet all of these requirements has been a great challenge

and has limited the development and large-scale implementation of hydrogen-generation processes by photoelectrochemical water splitting. An excellent review of tremendous advances in this field was reported by Navarro *et al.*⁵ Similarly, a perspective article by Duan *et al.*⁶ describes the catalytic mechanism of light-driven water oxidation in detail.

Ever since Fujishima and co-workers⁷ discovered that a rutile TiO₂ exhibits photo catalytic characteristics in 1972, titanium dioxide has shown an immense potential for water splitting. TiO₂ has several attractive physical-chemical properties that make it an excellent candidate for commercial water splitting: biocompatibility that simplifies disposal, excellent corrosion resistance and stability in most electrolytic solutions, relatively good optical absorption, and easiness to synthesize. However, the band gap of TiO₂ is relatively high (3.2 eV) and it is hence capable of absorbing only 5–7% of the solar spectrum.^{8–10} Extensive research has been undertaken by various groups to increase the photo-conversion efficiency of TiO₂ photoanodes. Grimes *et al.* have varied the morphology of the titania nanotubes (diameter, wall thickness, and height)¹¹ and thereby increased the surface roughness factor while Asahi and Morikawa¹² have doped nitrogen in order to alter its electronic properties and to reduce the bandgap. However, since only the top few

^a Nanotechnology Center, University of Arkansas at Little Rock, 2801 South University Avenue, Little Rock, AR 72204, USA. E-mail: gkkannarpady@ualr.edu, asbiris@ualr.edu; Fax: +1 501-683-7601, +1 501-683-7601; Tel: +1 501-569-8067, +1 501-551-9067

^b Applied Science and Technology, Sierra Lobo, ESC-24, Kennedy Space Center, FL 32899, USA

atomic layers of the titania surface come in direct contact with the electrolyte solution, we have recently reported an 80% increase in photo-conversion efficiency of titania nanotubes by using nitrogen plasma-assisted surface modification.¹⁰ Further, we have studied the effect of oxygen and nitrogen plasma treatment on the PEC properties of titania nanotubes.¹³

Similar to titania, WO₃ can be used as a potential photo-anode for water splitting. Unlike titania, the WO₃ has a much smaller band gap of 2.6 eV–2.9 eV and hence is capable of higher light absorption, about 12% of the solar spectrum;¹⁴ nevertheless, it suffers from relatively poor corrosion resistance. Thus far, however, not much effort has been devoted to realizing the potential of WO₃ for PEC applications and overcoming its limitations. Higashimoto *et al.* studied the PEC properties of the sputter-deposited WO₃ on titania substrates and showed that WO₃/TiO₂ hybrid structures have promising properties for photocatalytic cells. Chakrapani *et al.*¹⁵ synthesized a WO₃ nanowire using a hot wire chemical vapor deposition technique and studied its PEC properties using an acidic electrolyte. Although their results show reasonably good photocurrent response and stability, the acidic electrolytes could pose a much higher threat to chemical safety. Haidong *et al.* have reported the use of WO₃ thin films with nano-grains in dye-sensitized solar cells. Similarly, Tacconi *et al.*¹⁶ compared the PEC properties of titania nanotubes and WO₃ porous nanostructures in sodium sulfate electrolytes with and without sodium formate. Guo *et al.*¹⁷ investigated the PEC properties of WO₃ porous nanostructures and compared the results with the PEC properties of titania nanotubes. Their study showed that the photocurrent response of WO₃ nanostructures was superior to that of titania nanotubes. They further showed that WO₃ nanostructures suffered serious degradation under the acidic electrolyte. Recently, Hong *et al.*¹⁸ have generated a hetero-junction PEC cell of WO₃ along with BiVO₄ using a layer-by-layer deposition technique. The hetero-junction showed an enhanced photo-current conversion due to excellent charge transportation between BiVO₄ and WO₃.

The chemical nature of electrolytes plays a crucial role in the efficient functioning of a PEC solar cell. The interaction of the photoelectrodes at the interface of the surface and the electrolyte depends on the electrolyte pH, as well as the energy levels of the electrolytes and the electrodes. Raja *et al.*¹⁹ studied the photocurrent response of titania nanotubes in various electrolytes, and their findings revealed that the maximum photocurrent response was observed for KOH electrolytes. Similarly, it is interesting to study the photocurrent response of WO₃ porous nanostructures in various alkaline electrolytes including KOH. In this report, we have characterized WO₃ porous nanostructures for their PEC properties into three different alkaline electrolytes: (i) NaOH based, (ii) KOH based, and (iii) a mixture of NaOH and KOH based electrolytes. In addition, we compared the PEC properties of WO₃ porous nanostructures with those of titania nanotubes. While various photoanodes have already been characterized in KOH and NaOH electrolytes, to the best of our knowledge, this is the first time that a mixture of electrolytes containing KOH + NaOH has been proposed for photo-anodes to increase their PEC output. The observed results are discussed here based on

the energy level diagrams of the photo-electrode–electrolyte interface and the counter electrode. Moreover, we present a novel method to overcome the corrosion of the WO₃ electrodes in the electrolytes by coating their top surface with a 100 nm indium tin oxide (ITO) film. A tremendous increase in the photocurrent density, of as much as 340%, was observed for the nano-composite of ITO-coated, WO₃ porous nanostructures. Such coated WO₃ porous nanostructures could lead to a new type of multi-junction PEC cell along with titania nanotubes, with an enhanced absorption of the solar spectrum, to generate hydrogen *via* water splitting.

Materials and methods

Fabrication of TiO₂ nanotubes

Pure titanium foil (99.5% purity, 0.25 mm thickness, Alfa Aesar) was chemically etched using 100 ml phosphoric acid (H₃PO₄, Fischer scientific, 85% concentration) for 30 min at 80 °C to remove contamination on the surface. The etched samples were then rinsed with acetone, ethanol, and de-ionized (DI) water in an ultra-sonication bath for 5 min each. The cleaned samples were dried using dry nitrogen gas. TiO₂ nanotube arrays were fabricated using an in-house-built, two-electrode anodization technique. The cleaned Ti foil was used as the anode, and platinum (Pt, Sigma Aldrich, 99.9% purity) was used as the cathode. The distance between the anode and the cathode was maintained at 5 cm. The Ti foil sample was mounted on a Teflon holder with a hole (area 1.26 cm²) that exposes the sample to the anodization solution. The Pt cathode area was much larger (25 cm²) to ensure a uniform electric field between the anode and the cathode. The anodization was carried out using a mixture of 1.8 g ammonium fluoride (NH₄F) + 9 ml DI water + 441 ml ethylene glycol. In order to reduce the electrical resistivity of the electrolytic solution before anodizing the samples, a dummy Ti foil sample was subjected to anodization for 6 hours. Then the samples were anodized at a constant voltage of 20 V, for 60 min, at 50 °C with a continuous stirring of the solution. The elevated temperature enhances the fluoride ion activity and promotes better growth of TiO₂ nanotubes. After finishing the anodization process, the samples were rinsed with DI water for 5 min in the ultra-sonication bath and dried using dry nitrogen gas.

Fabrication of WO₃ porous nanostructures

Ti foil was used as the substrate to grow WO₃ porous nanostructures. First, the Ti foil was cleaned chemically as explained above. The substrates were mounted on a custom-made substrate holder attached to an in-house-built RF magnetron sputtering system. The chamber was pumped down to a base pressure of 5×10^{-7} Torr using a cryopump. Ar gas at a flow rate of 10 sccm was used to generate plasma with a chamber pressure of 10 mTorr. Tungsten (99.995%, ACI Alloys, CA) was deposited using a RF magnetron sputtering source with a power density of 5 W cm⁻². The substrate–target distance was maintained at 6", and the substrate temperature was maintained at 300 °C throughout the deposition. A thick layer of 1.45 microns of tungsten was deposited at a deposition rate of 0.1 Å s⁻¹. Similarly, tungsten was also deposited on a glass substrate with

the same deposition parameters for the purpose of SEM side-view imaging.

Tungsten oxide porous nanostructures were created on both the W-coated Ti- and W-coated glass substrates using the anodization technique explained above. An electrolytic solution comprising a mixture of 22.5 ml of DI water + 1.8 g NH_4F + 427.5 ml ethylene glycol was used for the anodization. The anodization potential was maintained at 35 V. Two sets of samples were prepared: one set with an anodization time of 1 hour and the other with an anodization time of 2 hours.

A nano-composite of WO_3 porous nanostructures and ITO was fabricated by coating a thin layer of ITO (100 nm) on the WO_3 porous nanostructures using a dc magnetron sputtering technique. The substrate was heated to 300 °C during the deposition of ITO to obtain high-quality ITO films.

Heat treatment

As-fabricated TiO_2 nanotubes and WO_3 nanostructures were amorphous in nature. To obtain the crystallinity of these samples, a heat-treatment at high temperature under an oxygen atmosphere was carried out. TiO_2 samples were mounted in a tubular furnace (2110, Barnstead Thermolyne) and heated to 600 °C using a temperature controller. The samples were annealed at this temperature for 2 hours under a constant flow of oxygen with a flow rate of 50 sccm. Similarly, WO_3 samples were annealed at two different temperatures under an oxygen atmosphere. The samples were annealed for 30 min at 350 °C followed by another 30 min of annealing at 500 °C. The oxygen flow rate was maintained at 50 sccm. Prior to the annealing of the samples, the furnace was cleaned with oxygen plasma for 10 min to remove organic contamination.

Surface morphology and surface chemistry

A Scanning Electron Microscope (JEOL 700) was used to view the nanostructures at higher magnification. The size and length of the nanostructures were determined by top-view and side-view SEM, respectively. X-Ray Photoelectron Spectroscopy (XPS) was used to characterize the chemical nature of tungsten oxide porous nanostructures. The XPS data were obtained on a Thermo Scientific K-Alpha X-ray photoelectron spectrometer at a background pressure of 1×10^{-9} Torr, using a monochromated $\text{Al K}\alpha$ ($h\nu = 1436.6$ eV) X-ray source. The X-ray beam used was 100 W, 400 μm in diameter. Survey scans (0–1350 eV) were taken of each sample at a pass energy (CAE) of 200 eV and 1 eV step size. The collected data were referenced

to the C1s peak at 284.6 eV. Narrow scans (25–40 eV width) of the peaks of interest (C1s , W4f) were taken at a pass energy of 50 eV and 0.1 eV step size to provide higher resolution analysis of the peaks. Curve fitting was performed on the narrow scans using the Advantage V. 4.38 software.

Photocurrent density measurement

The photocurrent response of TiO_2 and WO_3 nanostructure samples was measured using a standard three-electrode photo-electrochemical cell. TiO_2 and WO_3 nanostructure samples were used as working electrodes, or the photo anodes, with an exposure area of 1.0 cm^2 . A platinum foil (2.5 cm^2) was used as a counter electrode. A capillary tube filled with Ag/AgCl electrolyte and an insert of a salt-bridge (saturated KCl)-Luggin probe was used as a reference electrode. The photo anodes and the counter electrode were separated by a fine porous glass filter to prevent the recombination of hydrogen and oxygen molecules. The distance between the photo anodes and the Pt counter electrode was fixed at 10 cm. The solar spectrum was simulated using a xenon lamp (ACRO light, HID; 30 mW cm^{-2} power density), and the light was illuminated on the photo anode through an optical quartz window, with a diameter of 60 mm. In each case, the photocurrent density was measured using a potentiostat/galvanostat (Model283, EG&G instrument), with a potential held at a constant voltage of 0.7 V during both the dark (lamp OFF) and illumination (lamp ON) current measurements. The illuminated power density was measured by a radiometer (ILT14000A; International Light Technologies). Three sets of samples were tested for each oxide sample, and the average data were reported.

Results

WO_3 and TiO_2 nanostructures

Fig. 1 shows a SEM image of the nanotube arrays of TiO_2 generated by anodization that were used in this study as a standard comparative material for their PEC activity. The top view as seen from Fig. 1(a) clearly shows uniformly distributed TiO_2 nanotubes of diameter ~ 60 nm and ~ 7 nm in wall thickness. The morphology of the nanotubes is more evident in Fig. 1(b) which shows the side view of the nanotubes. As seen from the figure, the nanotubes are uniform in length, and their length as estimated from the side view was found to be ~ 1.3 μm .

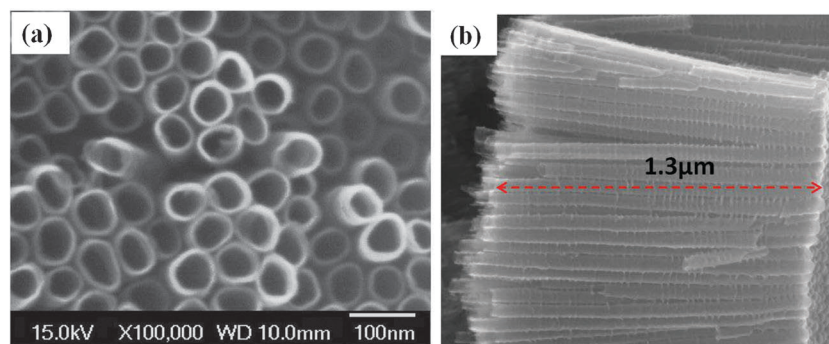


Fig. 1 Titania nanotube arrays generated by the anodization potential of 20 V for 1 hour; (a) top view and (b) side view.

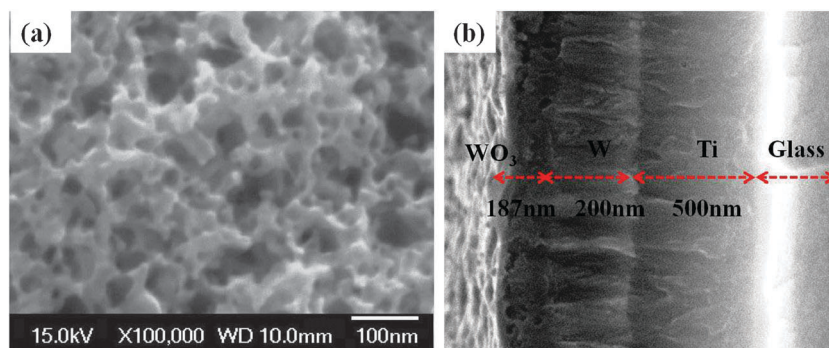


Fig. 2 WO_3 porous nanostructure generated by the anodization potential of 35 V for 1 hour; (a) top view and (b) cross-sectional view on a glass substrate.

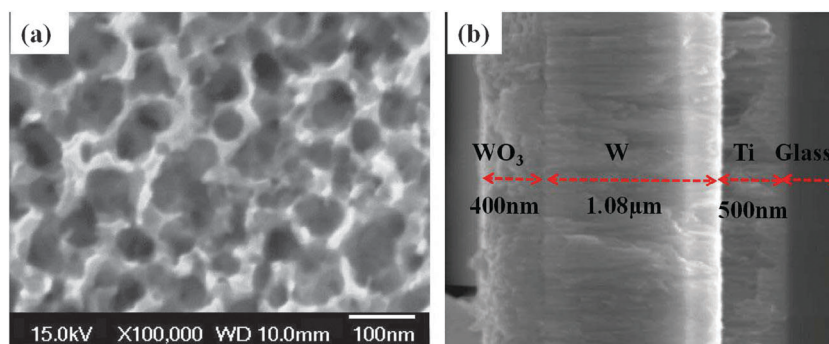


Fig. 3 WO_3 porous nanostructure generated by the anodization potential of 35 V for 2 hours; (a) top view and (b) cross-sectional view on a glass substrate.

On the other hand, the WO_3 samples present nano-porous “sponge-like” morphologies, as seen from the top view SEM image in Fig. 2. Although for our PEC property investigation we used WO_3 samples generated on a Ti substrate, for the cross-sectional morphology analysis we used a glass substrate for the fabrication of WO_3 nanostructures since cleaving the Ti substrate for side-view analysis was very difficult. Fig. 2 shows the WO_3 nanostructures corresponding to one hour of anodization. The top view indicates that the size distribution of the nanoporous structures ranged between ~ 20 nm to ~ 50 nm. The height of the nanostructures was approximately 190 nm as seen from the cross-sectional view. Similarly, Fig. 3 shows both top and cross-sectional views of WO_3 nanostructures after 2 hours of anodization. The increase in the anodization time resulted in much taller nano-porous structures, 400 nm as determined from Fig. 3(b), with a fairly uniform distribution. The diameter of nano-porous structures was also found to increase to ~ 60 nm as opposed to ~ 20 – 50 nm for the one-hour anodized sample. The surface roughness was measured by an atomic force microscope (AFM) for both the one-hour and two-hour WO_3 samples; their surface roughness was found to be 10.45 nm and 18.78 nm, respectively. This indicates that the increase in anodization time increases the surface area.

XPS analysis

Fig. 4(a) shows a high resolution XPS spectrum of the $\text{W}4f_{7/2}$ and $\text{W}4f_{5/2}$ peaks of a tungsten standard (Geller Micro Analytical, MA). The sample was etched with an argon ion

beam prior to analysis to remove any residual oxide layer and contaminants. The $\text{W}4f_{7/2}$ peak was determined to be at 31.0 eV, corresponding to metallic tungsten as expected.^{20,21} Fig. 4(b) shows a high resolution XPS spectrum of the $\text{W}4f_{7/2}$ and $\text{W}4f_{5/2}$ peaks of the sample nanostructures. In this spectrum, the $\text{W}4f_{7/2}$ peak was determined to be at 35.80 eV, corresponding to that of WO_3 .^{20,21} The free energy of formation $\Delta_f G^\circ$ (298 K) of WO_2 and WO_3 is -533.9 and -764.0 kJ mol $^{-1}$, respectively,²² indicating that the formation of WO_3 was the more favorable and stable process with our samples.

PEC characterization of WO_3 nanostructures and TiO_2 nanotubes

The photocurrent response of both TiO_2 and WO_3 nanostructures was measured using a PEC cell with three different electrolytes. The first one, referred to as Electrolyte A, was a combination of 0.5 M NaOH + 10 vol% EG + DI water. Similarly, the second one, Electrolyte B, was composed of 0.3 M KOH + 10 vol% EG + DI water. The third electrolyte, Electrolyte C, was a mixture of Electrolyte A and Electrolyte B (0.5 M NaOH + 0.3 M KOH + 10 vol% EG + DI water). Initially, 0.7 V potential was applied between the reference electrode and the counter electrode using the potentiostat and the stability of the applied voltage was tested for 10 min under both xenon lamp ON/OFF conditions. The dark photocurrent density was measured with the lamp OFF. The observed dark photocurrent density was found to be less than 40 $\mu\text{A cm}^{-2}$ for all of the electrolytes. Afterwards, the photocurrent density of titania nanotube arrays was measured with xenon lamp ON

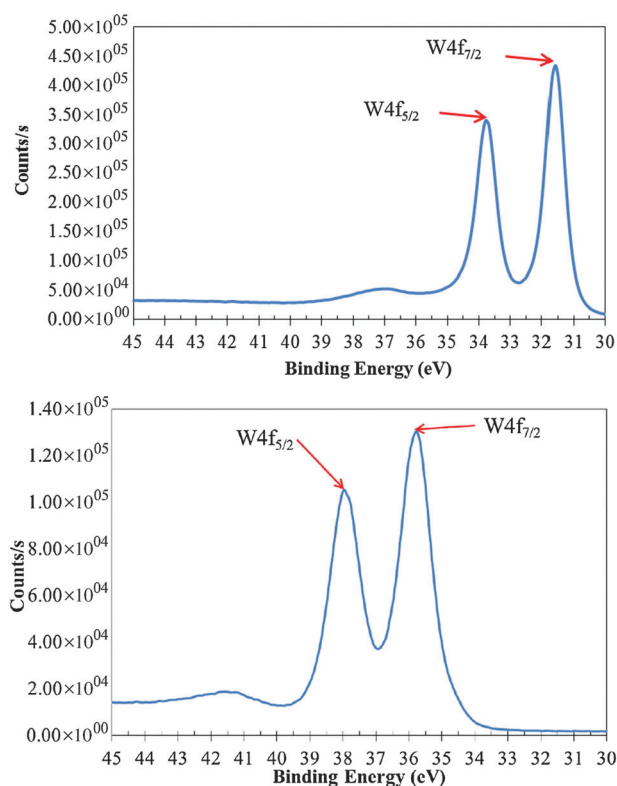


Fig. 4 (a) XPS spectrum of reference W foil. (b) XPS spectrum of WO₃ porous nanostructures.

for a period of 5 minutes. The results were recorded using a computer as a function of time for each electrolyte. Fig. 5 shows the variation of the photocurrent density as a function of time for the titania nanotube arrays and the different electrolytes. As seen from the plot, a clear spike in the photocurrent density was observed for all three electrolytes as soon as the lamp was turned ON. This is because the xenon lamp showed a much higher power density (65 mW cm^{-2}) in the beginning before stabilizing at 30 mW cm^{-2} . After the power density stabilized, a plateau of photocurrent density (PPCD) was observed throughout the time period of the lamp ON. Interestingly, the highest PPCD was observed for Electrolyte C, the mixture of Electrolytes A and B: approximately 65% more than that for Electrolyte A and 43% more than that for Electrolyte B.

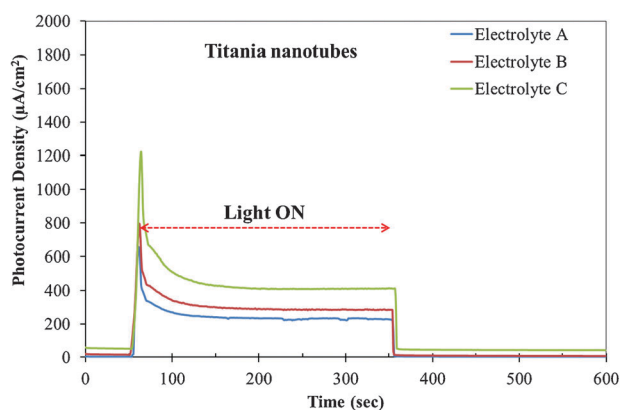


Fig. 5 Photocurrent density as a function of time for titania nanotubes in the different electrolytes.

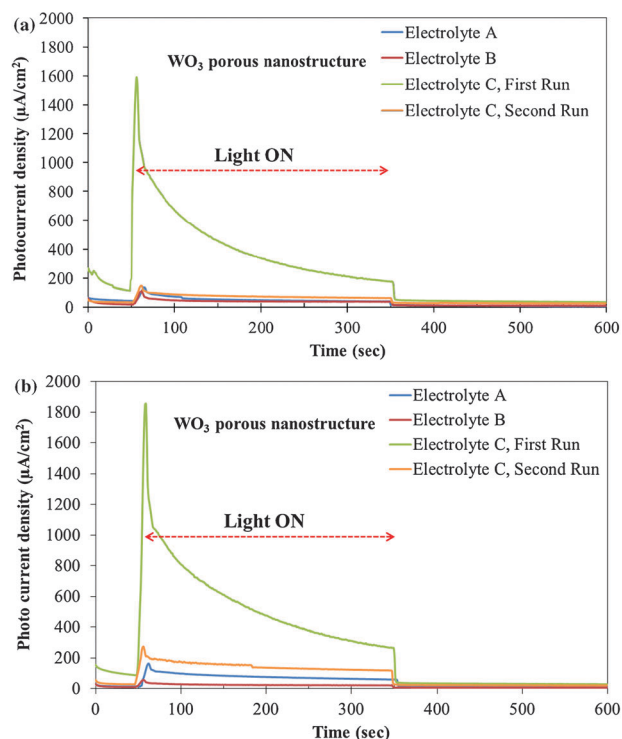


Fig. 6 (a) Photocurrent density as a function of time for WO₃ porous nanostructures (1 hour sample) in the different electrolytes. (b) Photocurrent density as a function of time for WO₃ porous nanostructures (2 hour sample) in the different electrolytes.

Similarly, photocurrent density vs. time was measured for both the one-hour and two-hour WO₃ nano-porous structures. The photocurrent response of the one-hour sample is shown in Fig. 6(a). As seen from the figure, the photocurrent response for Electrolytes A and B was very similar to that of titania nanotubes, although the PPCD was relatively lower than that for the titania nanotubes. For Electrolyte C, we conducted two runs of photocurrent density measurement. During the first run, a fairly high photocurrent density of $150 \mu\text{A cm}^{-2}$ was observed even under the lamp OFF condition. When the sample was illuminated, the photocurrent increased abruptly to $1600 \mu\text{A}$ due to the initial increase in the power density of the lamp. Eventually, the current output decreased as the lamp power stabilized at 30 mW cm^{-2} . The observed photocurrent was higher than that for titania nanotubes, although a gradual decrease in the current was observed as a function of time. For the second run, the trend was similar to the first, but the photocurrent output was much lower. Also, the sample surface color changed from blue to yellow. Similarly, for the two-hour nano-porous WO₃ sample, the photocurrent response as a function of time is shown in Fig. 6(b). The responses for all of the electrolytes were very similar to that of the one-hour sample.

Fig. 7 shows the photocurrent response of the ITO-coated, WO₃ nanostructures. A tremendous increase in photocurrent density was observed for the ITO-coated samples during the first run as seen in Fig. 7(a). However, the current density decreased gradually as a function of time. For the second run, the photocurrent density was much lower than that for the first run but still higher than that for the second run of the samples without ITO as seen in Fig. 7(b).

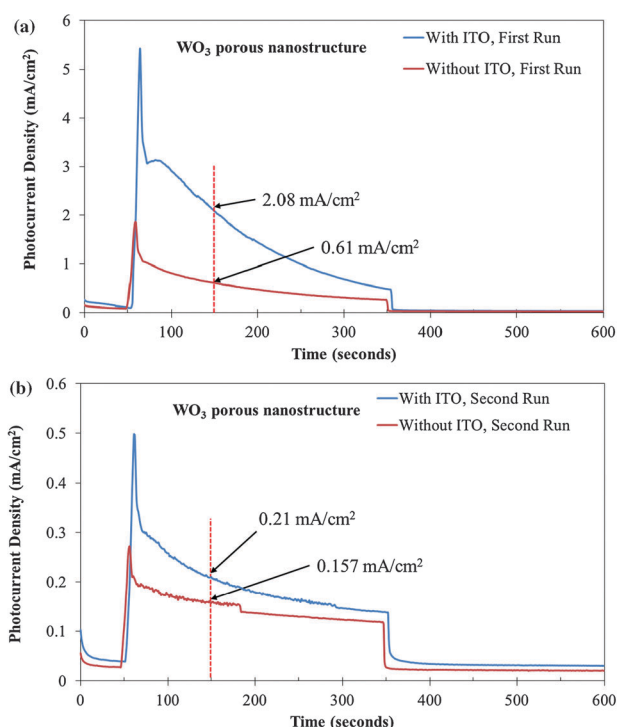


Fig. 7 Photocurrent density as a function of time for ITO-coated, WO_3 porous nanostructures (1 hour sample) in Electrolyte C, (a) for the first run and (b) for the second run.

Discussion

PEC response of titania nanotubes

The photocurrent response of semiconducting materials in electrolytes can be understood using energy level diagrams of the semiconductor–electrolyte interface and the metal counter electrode. A conceptual energy level diagram, based on the earlier work,^{19,23} for the titania nanotube–electrolyte interface and the Pt counter electrode is shown in the left side of Fig. 8(a). As seen from the figure, when titania nanotubes come in contact with the electrolytes, bending of the band gap occurs, resulting in the equilibrium of energy levels, with the Fermi level close to $E_{\text{O}_2/\text{H}_2\text{O}}$ and the valence band under the lamp OFF condition. Upon illumination, as seen in the right side of Fig. 8(a), the holes generated by the light excitation move to the surface and recombine with the electrons available in $\text{O}_2/\text{H}_2\text{O}$ resulting in oxygen evolution. On the other hand, the electrons from the conduction band move to the Pt counter electrode through the external circuit, measured as the photocurrent density. Further, the electrons facilitate the hydrogen generation when they reach water. The amount of hydrogen generated and the registered photocurrent depend on the intensity of the illuminated light.

For the titania nanotubes, much lower PPCD was observed for Electrolyte A compared to Electrolyte B, which could be explained by the formation of sodium titanate on the surface of the titania nanotubes in Electrolyte A, as previously reported by Oh *et al.*²⁴ This process of sodium titanate formation over the titania nanotube surface could significantly shield the absorption of the illuminated light. As explained above, the amount of photocurrent generated depends on the intensity of

the illuminated light; hence, a reduction in the photocurrent density output was observed for Electrolyte A. A similar trend has been observed by Raja *et al.* for titania nanotubes.¹⁹ However, interestingly, Electrolyte C, which contained a mixture of NaOH and KOH, produced the highest PPCD. This may be explained based on the reduction in electron–hole recombination. While the intensity of the light controls the photocurrent output, the electron–hole recombination process also plays a major role in determining the output photocurrent. The higher the electron–hole recombination, the lower the photocurrent output. It is established that the OH^- ions produced during electrochemical reaction can avoid the electron–hole recombination.^{25,26} The amount of OH^- ions available in the mixture of NaOH + KOH (Electrolyte C) was much higher than that for either KOH (Electrolyte B) or NaOH (Electrolyte A). Hence, the higher concentration of OH^- ions may have reduced the electron–hole recombination, yielding higher PPCD for the Electrolyte C.

PEC response of WO_3 porous nanostructures

As noted earlier, WO_3 nanostructures show a completely different trend of photocurrent response in comparison with titania nanotubes. In this case, the Electrolyte A containing NaOH generated a much higher current than Electrolyte B. Also, Electrolyte C showed a non-plateau photocurrent response during the lamp ON for 5 min. As is well known,^{27,28} KOH is a very good etchant for many materials including tungsten oxide. Hence, the observed PPCD for the KOH electrolyte was lower as KOH etches WO_3 and thereby reduces the absorption of the illuminated light.

On the other hand, for the mixture of NaOH and KOH electrolytes, a non-plateau photocurrent response was observed. A hypothetical energy level diagram for a WO_3 –Electrolyte C interface and a Pt counter electrode is shown in Fig. 8(b). Along with the $\text{O}_2/\text{H}_2\text{O}$ energy level, an additional energy level for H_xWO_y ²⁹ is hypothetically possible. For the KOH and NaOH mixture, the H_xWO_y translates into K_xWO_3 ^{30,31} and Na_xWO_4 compounds. The position of these energy levels with respect to the Fermi level dictates the decomposition of the H_xWO_y compounds. If the additional energy level falls above the $\text{O}_2/\text{H}_2\text{O}$ level and close to the Fermi level, the decomposition takes place with the generation of $(\text{WO}_4)^{2-}$ ions.²⁹ These ions inhibit electron–hole recombination in a manner similar to $(\text{OH})^-$ ions.^{32,33} Since the observed photocurrent density for WO_3 nanostructures in Electrolyte C was higher than that for the titania nanotubes for the first run, we hypothesize that the H_xWO_y energy level is near the Fermi level and above the $\text{O}_2/\text{H}_2\text{O}$ level under equilibrium conditions as shown in Fig. 8(b). Upon illuminating the lamp, corresponding to the right side of Fig. 8(b), the hole–electron transport mechanism takes place, similar to the titania nanotubes as explained above. However, the electron–hole recombination was greatly reduced in this case as the additional electron–hole recombination inhibitor, the $(\text{WO}_4)^{2-}$ ions, was available along with $(\text{OH})^-$ ions. Hence, higher photocurrent density was observed for WO_3 nanostructures for the first run. However, the KOH in Electrolyte C reduced the amount of the illuminated light absorption. Hence, the photocurrent response of WO_3 was non-plateau with a gradual decrease in photocurrent density

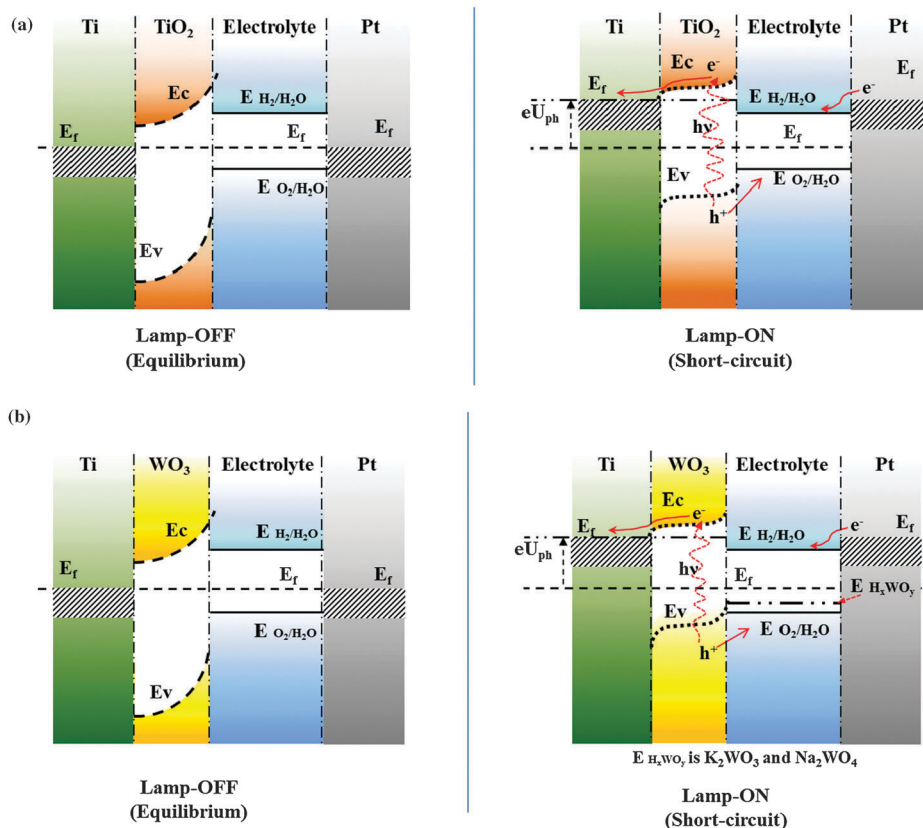


Fig. 8 (a) A conceptual energy level diagram of a titania nanotube–electrolyte interface and a Pt counter electrode based on the work of Raja *et al.*¹⁹ (b) A hypothetical energy level diagram of a WO₃–electrolyte interface and a Pt counter electrode.

as a function of time. Similarly, for the second run, a huge reduction in the photocurrent response was observed, as shown in Fig. 6(b), due to a decrease in the illuminated light absorption due to the surface etching.

PEC response of ITO coated WO₃ porous nanostructures

As discussed previously, WO₃ porous nanostructures demonstrated non-plateau photocurrent response due to the surface degradation in all of the electrolytes. We propose an electrically conducting but optically transparent protective coating on WO₃ porous nanostructures to prevent them from being corroded under the electrolytes. However, the selection of such a protective layer should not impede the PEC capabilities of the nanostructural films. The band gap of the protective layer must be higher than that of WO₃ with the conduction band of the protective layer positioning above the conduction band of WO₃. Hence, we selected ITO as the protective layer, since it is both electrically conducting and optically transparent. The band gap of ITO is in the vicinity of 4.7 eV,³⁴ and its conduction band falls above the conduction band of WO₃ as shown in Fig. 9. Moreover, ITO is highly stable under the alkaline electrolytes.³⁵ As noted earlier, from Fig. 7(a), a 340% increase in the photocurrent density was observed for the ITO-coated samples. The lamp used to illuminate the light takes 100 s to stabilize its power to 30 mW cm⁻² from its initial value of 65 mW cm⁻² as soon as it is turned ON. Hence, we compared the values of the photocurrent density at 100 s after

the lamp was ON. The photocurrent density decreased as a function of time, similar to the sample without ITO coating, possibly due to the non-conformal coating of ITO. We used a dc magnetron sputtering technique to deposit ITO on the porous nanostructures. Although the sputtering technique can deposit materials on the sidewall of the features, the technique is not as efficient in covering the sidewalls conformally, especially with high-aspect ratio features. Since the diameter of porous nanostructures is very small, in the range of 20–50 nm, the aspect ratio of the features is very high. The spots lacking ITO coating on the sidewalls of porous nanostructures could act as etching centers when the samples come in contact with the electrolytes. As a result, surface etching can take place through the sidewalls, although at a slower rate than that for the samples without ITO coating. Hence, the samples coated with ITO show a tremendous increase in the photocurrent response due to the reduced etching rate. Nevertheless, due to the sidewall etching, the photocurrent density reduces gradually as a function of time, and more work will be required to fully overcome the degradation limitation. The effect of ITO in reducing the etching rate was also evident from the higher photocurrent density for the second run than that for the second run of the sample without ITO coating as seen in Fig. 7(b). However, at the end of the second run, the photocurrent density for the ITO coated WO₃ sample was almost the same as that for the sample without ITO coating. Although, we have proved our concept of improving photo catalytic activity of WO₃ by coating ITO, further improvement has to be made in

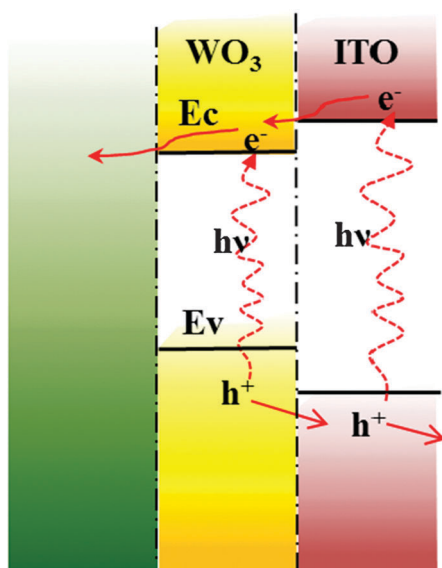


Fig. 9 Energy level diagram for a WO₃-ITO nano-composite.

depositing ITO conformally on WO₃ porous nanostructures to achieve a stable enhanced photo catalytic behavior over a long period of time for any practical applications.

Conclusions

The PEC properties of WO₃ porous nanostructures were compared with those of titania nanotubes in three alkaline based electrolytes. Although WO₃ porous nanostructures showed poor corrosion resistance in all of the three electrolytes that were used for this study, they exhibited much higher photocurrent response in the electrolyte that contained a mixture of NaOH and KOH than that for titania nanotubes. XPS analysis confirmed that we successfully generated WO₃ porous nanostructures. A hypothetical energy level diagram for a WO₃ porous nanostructure-electrolyte interface and a Pt counter electrode was proposed to understand the PEC properties. A novel nano-composite of ITO and WO₃ porous nanostructures was fabricated by coating with a thin layer of ITO. A significant reduction in the surface etching was observed for the nano-composite structures in the alkaline electrolytes resulting in a tremendous increase (340%) in the photocurrent response. The promising PEC results of ITO/WO₃ composite nanostructures indicate, along with titania nanotubes, that a tandem multi-junction PEC cell could be constructed for an enhanced absorption of the solar spectrum for water splitting to generate hydrogen.

Acknowledgements

Financial support from Department of Energy (DE-FG36-06GO86054), U.S. Army (ERDC Cooperative Agreement Number: W912HZ-09-02-0008), Arkansas Science & Technology Authority (Grant # 08-CAT-03), Department of Energy (DE-FG36-06GO86072), and National Science Foundation (NSF/EPS-1003970) is greatly appreciated. The editorial assistance of Dr Marinelle Ringer is also acknowledged.

References

- 1 E. L. Miller, R. E. Rocheleau and X. M. Deng, *Int. J. Hydrogen Energy*, 2003, **28**, 615–623.
- 2 C. Burda, Y. Lou, X. Chen, A. C. S. Samia, J. Stout and J. L. Gole, *Nano Lett.*, 2003, **3**, 1049–1051.
- 3 V. K. Mahajan, S. K. Mohapatra and M. Misra, *Int. J. Hydrogen Energy*, 2008, **33**, 5369–5374.
- 4 W. Siripala, A. Ivanovskaya, T. F. Jaramillo, S.-H. Baeck and E. W. McFarland, *Solar Energy Mater. Solar Cells*, 2003, **77**, 229–237.
- 5 R. M. Navarro, M. Alvarez-Galvan, I. M. Villoria de, S. Al-Zahrani and J. L. G. Fierro, *Energy Environ. Sci.*, 2010, **3**, 1865–1882.
- 6 L. Duan, L. Tong, Y. Xu and L. Sun, *Energy Environ. Sci.*, 2011, **4**, 3296–3313.
- 7 A. Fujishima and K. Honda, *Nature*, 1972, **238**, 37–38.
- 8 H. Irie, Y. Watanabe and K. Hashimoto, *J. Phys. Chem. B*, 2003, **107**, 5483–5486.
- 9 S. K. Mohapatra, M. Misra, V. K. Mahajan and K. S. Raja, *J. Phys. Chem. C*, 2007, **111**, 8677–8685.
- 10 R. Sharma, P. P. Das, M. Misra, V. Mahajan, J. P. Bock, S. Trigwell, A. S. Biris and M. K. Mazumder, *Nanotechnology*, 2009, **20**, 075704.
- 11 M. Paulose, K. Shankar, S. Yoriya, H. E. Prakasham, O. K. Varghese, G. K. Mor, T. A. Latempa, A. Fitzgerald and C. A. Grimes, *J. Phys. Chem. B*, 2006, **110**, 16179–16184.
- 12 R. Asahi and T. Morikawa, *Chem. Phys.*, 2007, **339**, 57–63.
- 13 H. Ishihara, J. P. Bock, R. Sharma, F. Hardcastle, G. K. Kannapady, M. K. Mazumder and A. S. Biris, *Chem. Phys. Lett.*, 2010, **489**, 81–85.
- 14 D. W. Bullett, *J. Phys. C: Solid State Phys.*, 1983, **16**, 2197.
- 15 V. Chakrapani, J. Thangala and M. K. Sunkara, *Int. J. Hydrogen Energy*, 2009, **34**, 9050–9059.
- 16 N. R. de Tacconi, C. R. Chenthamarakshan, G. Yogeeswaran, A. Watcharenwong, R. S. de Zoysa, N. A. Basit and K. Rajeshwar, *J. Phys. Chem. B*, 2006, **110**, 25347–25355.
- 17 Y. Guo, X. Quan, N. Lu, H. Zhao and S. Chen, *Environ. Sci. Technol.*, 2007, **41**, 4422–4427.
- 18 S. J. Hong, S. Lee, J. S. Jang and J. S. Lee, *Energy Environ. Sci.*, 2011, **4**, 1781–1787.
- 19 M. Misra, K. S. Raja and V. K. Mahajan, *J. Power Sources*, 2006, **159**, 1258–1265.
- 20 D. Briggs and M. P. Seah, *Practical surface analysis: Volume 1—Auger and X-ray Photoelectron Spectroscopy*, Wiley, Chichester, c1990–c1992.
- 21 J. Chastain and J. F. Moulder, *Handbook of X-ray photoelectron spectroscopy: a reference book of standard spectra for identification and interpretation of XPS data*, Physical Electronics Division, Perkin-Elmer Corp., Eden Prairie, Minn., 1992.
- 22 D. R. Lide, *CRC Handbook of Chemistry and Physics*, CRC press Inc, Boca Raton, FL, 82nd edn, 2002.
- 23 R. Memming, *Electrochim. Acta*, 1980, **25**, 77–88.
- 24 S. Oh, R. R. Finões, C. Daraio, L. Chen and S. Jin, *Biomaterials*, 2005, **26**, 4938–4943.
- 25 J. L. Cao, Z. C. Wu and J. Q. Zhang, *J. Electroanal. Chem.*, 2006, **595**, 71–77.
- 26 O. Carp, C. L. Huisman and A. Reller, *Prog. Solid State Chem.*, 2004, **32**, 33–177.
- 27 L. A. Hockett and S. E. Creager, *Rev. Sci. Instrum.*, 1993, **64**, 263–264.
- 28 B. Munro, S. Kramer, P. Zapp and H. Krug, *J. Sol-Gel Sci. Technol.*, 1998, **13**, 673–678.
- 29 A. Enesca, L. Andronic, A. Duta and S. Manolache, *International Semiconductor Conference*, 2006, **2**, 241–244.
- 30 R. J. D. Tilley, *Int. J. Refract. Met. Hard Mater.*, 1995, **13**, 93.
- 31 M. Gillet, R. Delamare and E. Gillet, *J. Cryst. Growth*, 2005, **279**, 93–99.
- 32 C. A. Grimes, C. Ruan, M. Paulose and O. K. Varghese, *Solar Energy Mater. Solar Cells*, 2006, **90**, 1283–1295.
- 33 H. Cheng and A. Selloni, *Langmuir*, 2010, **26**, 11518–11525.
- 34 B. Yu, A. Tsai, S. Tsai, K. Wong, Y. Yang, C. Chu and J. Shyue, *Nanotechnology*, 2008, **19**, 255202.
- 35 S. Gardonio, L. Gregoratti, D. Scaini, C. Castellarin-Cudia, P. Dudin, P. Melpignano, V. Biondo, R. Zamboni, S. Caria and M. Kiskinova, *Org. Electron.*, 2008, **9**, 253–261.